Nonlocal spin transport based on a half-metallic ferromagnet

Yao Junxiang [1,*] Prateek Kumar,[1] Mariona Cabero-Piris,[2] and Jan Aarts [1,†]
[1]Huygens-Kamerlingh Onnes Laboratory, Leiden Institute of Physics, Leiden University, P.O. Box 9504, 2300 RA Leiden, Netherlands
[2]ICTS - Centro Nacional de Microscopía Electrónica, Universidad Complutense de Madrid, 28040 Madrid, Spain

(Received 22 January 2023; revised 4 August 2023; accepted 22 August 2023; published 24 October 2023)

We study the spin injection from the ferromagnetic metallic oxide $La_{0.7}Sr_{0.3}MnO_3$ (LSMO) into the normal metal Ag. LSMO is a highly resistive metallic oxide, but also fully spin polarized and therefore holds promise of generating highly polarized spin currents. Because of the high resistivity of the ferromagnet, and the lower resistivity of the normal metal, no conductivity mismatch issues are expected, as we demonstrate with model calculations. Our measurements unambiguously show spin-coherent injection and detection. LSMO appears to be a useful material for spin injection, but we also find the presence of an intrinsic tunnel barrier and a lower-than-expected degree of spin polarization, indicating a spin-active interface.

DOI: 10.1103/PhysRevMaterials.7.104408

I. INTRODUCTION

Spin holds promise for the application in next-generation memory devices with the low-power operation and multiple functionalities [1,2]. Pure spin transport, without accompanying charge transport, is driven by spin chemical potential difference, similar to the way charge is transported by an electric potential. Spin transport leads to similar phenomena as charge transport, such as a spin Hall effect [3] or spin thermal effects [4] with the important caveat that, unlike charge, spin is not a conserved quantity. Spin currents therefore decay under influence of spin-flip processes, over some characteristic length λ. How to generate pure spin currents has been the subject of much research over the last decade. One method is to inject spins (and charge) from a ferromagnet F into another metal or semiconductor [5–10]. Another is to use ferromagnetic resonance to accumulate spins on the normal (N) side of an F/N interface [11–14].

A widely-used geometry to study spin injection and spin currents is a lateral spin valve geometry, in which two ferromagnetic bars (F_1 and F_2), at a distance L and with the controllable direction of their magnetization, are connected by an N wire. The geometry is schematically shown in Fig. 1(a) [6,15,16]. When charge current flows from F_1 (the injector) to N, spins are injected into the normal metal and start to diffuse through the current-free part of the wire, resulting in pure spin current transport driven by a spin chemical potential difference, and decaying because of spin-flip processes. This spin current can be detected by F_2 (the detector) by measuring the (nonlocal) voltage difference between N and F_2, which depends on the relative magnetization directions of F_1 and F_2. When they are parallel (P), there is no barrier for spin transmission and no voltage, but in the antiparallel case (AP), spin transmission is impeded and a voltage develops. A condition for a detectable signal is that the spacing between the injector and detector is smaller than the spin diffusion length of the N metal. The geometry then allows analyzing the injected amount of spin polarization and the relevant spin lifetime or spin diffusion length by solving the one-dimensional spin diffusion equation [3,6,15,17–20].

A critical problem in spin injection lies in the interface resistance R_{int} between F_1 and N, but also in the ratio of the conductivities σ_F of the F_1 layer and σ_N of the N layer [21–25]. Detailed calculations by Schmidt *et al*. [21] showed that, even in the case that the bulk spin polarization of the ferromagnet P_F is very high, say 90%, the spin polarization P of the injected current is below 0.1% for a conductivity ratio (σ_F/σ_N) of 100 (when N actually is a semiconductor), and still not more than 0.05 when the ratio is 1. Conductivity mismatch is very detrimental to injection efficiency. Moreover, the small amount of injected P makes the resistance difference between the antiparallel and parallel states relative to the parallel state, expressed as $\Delta R/R_P$, also very small (10^{-7} and thus not detectable as a nonlocal signal in the semiconductor case).

The proposed solution is inserting a tunnel barrier between F_1 and N, to eliminate the conductivity mismatch artificially [7,22]. Fukuma *et al.* [19] reported that a specially prepared MgO tunnel barrier can enhance the spin injection significantly and lead to a 100-fold increase of nonlocal signal. However, the spin injection efficiency is not merely positively correlated with the interface resistance. With increasing resistivity of the tunnel barrier, spin relaxation effects become more pronounced, resulting in a decrease of spin injection efficiency. Godfrey *et al*. [25] and Kimura *et al*. [15], independently, found a quite large spin accumulation in the Py/Ag system with transparent interfaces and concluded that a low or moderate interface resistance is sufficient for high spin injection in certain systems. Therefore, it is indispensable to consider both the conductivity ratio (σ_F/σ_N) and interface resistance R_{int} to understand the characteristics of spin transport in specific materials systems.

In this paper, we investigate the injection efficiency of a fully spin-polarized metallic oxide, the manganite $La_{0.7}Sr_{0.3}MnO_3$(LSMO), into a normal metal (Ag). The

*yao@physics.leidenuniv.nl
†aarts@physics.leidenuniv.nl

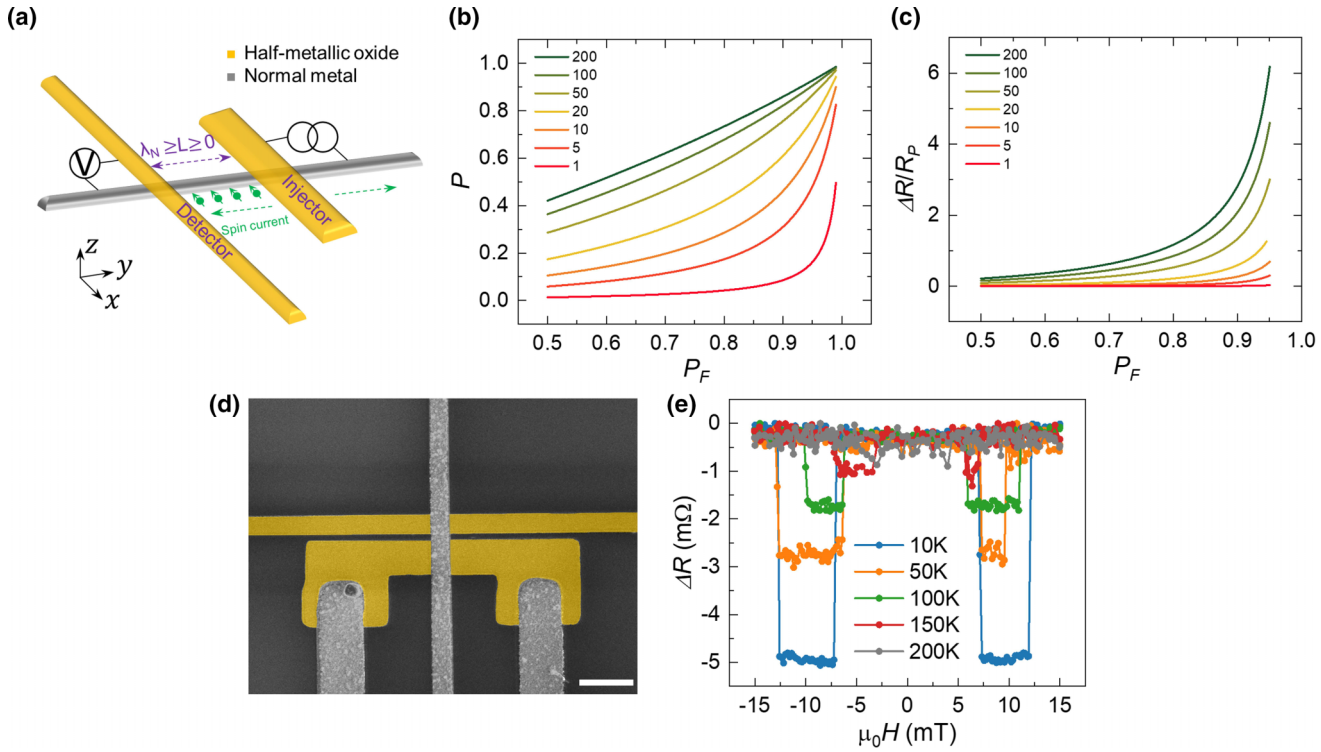

FIG. 1. Nonlocal spin transport in a half-metallic oxide/normal metal system. (a) Schematic illustration of the lateral spin valve. (Note the IP parallel field is along the x axis, and the IP longitudinal field is along the y axis, as depicted in the coordinate system.) (b) Spin polarization of the injected current P as a function of the spin polarization of the half-metallic oxide P_F for different conductivity ratios (σ_N/σ_F) as indicated. (c) The nonlocal signal normalized by the resistance in the parallel state $\Delta R/R_P$ as function of P_F. (d) A false-colored scanning electron microscopy image displaying the nonlocal device consisting of an LSMO nanowire (detector) and an LSMO nanowire with pad (injector), bridged by a Ag nanowire; the detector and injector are highlighted in yellow. The scale bar is 2.5 μm. (e) Temperature-dependent ΔR measurements on a device with a spacing $L = 173$ nm. All curves are manually shifted to the same baseline for comparison.

resistivity of these oxides is high, the conductivity ratio σ_F/σ_N is of order 0.1 to 0.01, and a mismatch problem should not occur. Manganites are well-known half-metals and have been widely studied in magnetic tunnel junctions [26,27]. Somewhat surprisingly, they have not been much researched in conjunction with spin injection. Spin pumping by ferromagnetic resonance was reported for the LSMO/Pt bilayer system [28,29], where it was remarked that the data indicate spin-memory loss at the interface [29]. LSMO was also used for spin injection in graphene [30]. Long spin diffusion lengths were observed, but the signals were low, due to the high interface resistance.

The issues of spin-memory loss and interface resistance are of generic interest when using LSMO or similar oxides in spintronics applications, including superconductivity (superspintronics). Therefore, we selected the LSMO/Ag system for a detailed study of the half-metallic oxide/normal metal model in the nonlocal configuration. Ag has a relatively weak spin-orbit interaction (SOI) [15,19,31]. By performing nonlocal voltage measurements on two-bar devices, where P and AP magnetization configurations can be prepared by in-plane (IP) magnetic fields, we show that a nonlocal spin signal exists and endures up to 200 K, which is correlated with the magnetic behavior of the LSMO nanostructures. We also use out-of-plane (OP) fields to induce (Hanle) spin precession. With help of these data, we demonstrate that in our devices LSMO induces a spin polarization P of the injected current ≈11.6%, allowing to measure a spin diffusion signal in the Ag nanowire of more than 1 μm at 10 K. The extracted transverse spin relaxation time T_2 is about 66 ps, in reasonable agreement with the longitudinal-spin relaxation time $T_1 \approx 70$ ps, as obtained by fitting the spatial dependence of the nonlocal spin transport. The discrepancy between the experiment and theory is discussed within the tunneling regime, appropriate for the various (spin) resistance values, and allows the conclusion that the interface contains a spin-active layer. Following up on this conclusion we present scanning transmission electron microscopy (STEM) data that make this conclusion plausible.

II. HALF-METALLIC OXIDE/NORMAL METAL LATERAL SPIN VALVES

First, we theoretically investigate what can be expected when measuring spin transport in the nonlocal geometry described above, for the case of a half-metallic oxide (HM)/normal metal (N) system. In such a case, the bulk spin polarization P_F of both injector and detector is much higher than of conventional ferromagnets where $P_F \approx 0.5$. Also, the conductivity ratio between a normal metal and half-metallic oxide (σ_N/σ_{hm}) is of order 100, which is 10^2 times larger than for conventional ferromagnets, where $\sigma_N/\sigma_F \approx 1$. In this limit, we are far from the detrimental effects of the earlier-mentioned conductivity mismatch.

We use the description of Schmidt *et al*. [21] for a transparent interface without spin scattering or interface resistance, and an infinite spin diffusion length λ_N in the normal metal. In that case the spin polarization P of the injected current is described by the following formula:

$$P = P_F \frac{\lambda_F}{L} \frac{\sigma_N}{\sigma_F} \frac{2}{\left(2\frac{\lambda_F \sigma_N}{L \sigma_F} + 1\right) - P_F^2}, \quad (1)$$

where P_F and λ_F are the spin polarization and spin diffusion length of the ferromagnet, respectively, and the other quantities already have been introduced. Figure 1(b) shows a calculation of P as function of P_F, using Eq. (1), for $\lambda_F = 10$ nm, $L = 1$ μm, and different conductivity ratios. For $\sigma_N/\sigma_F = 100$ we find $P = 0.9$, while for $\sigma_N/\sigma_F = 10$, P is still larger than 0.2, much larger than what can be expected for a normal metal with a conventional ferromagnet. Calculations of P for different values of λ_F and L are given in Fig. S1 within the Supplemental Material (SM) [32]. Basically, and without considering spin relaxation effects at interfaces or surfaces [18,31,33,34], high spin polarization values are expected in a HM/N system.

Another useful parameter to consider is the size of the nonlocal signal $(R_P - R_{AP})/R_P = \Delta R/R_P$ where the resistance $R_{P,AP}$ is defined as the nonlocal voltage in the P or AP configuration divided by the injection current. The resistance change ΔR is also called the spin accumulation signal or the spin resistance R_s, but since ΔR is measured, we stay with that quantity for the moment. Following Ref. [21], $\Delta R/R_P$ is given by

$$\frac{\Delta R}{R_P} = \frac{P_F^2}{1 - P_F^2} \frac{\lambda_F^2}{\sigma_F^2} \frac{{\sigma_N}^2}{L^2} \frac{4}{\left(2\frac{\lambda_F \sigma_N}{L \sigma_F} + 1\right)^2 - P_F^2}. \quad (2)$$

We calculated the ratio $\Delta R/R_P$ as a function of the bulk spin polarization P_F. Figure 1(c) shows the nonlocal spin signal is easily measurable electrically with $\sigma_N/\sigma_F = 10$ and $\lambda_F = 10$ nm at $L = 1$ μm, in comparison to the unreachable 10^{-7} in the conventional ferromagnet/semiconductor system [21]. As long as $P_F \geqslant 0.8$, the nonlocal spin signal is detectable, which would be the case for a half-metallic oxide. In Fig. S1c within the SM [32] a calculation is given for $P_F = 0.96$ and $\lambda_F = 10$ nm, revealing that $\Delta R/R_P$ is always measurable experimentally. On the whole, the calculations indicate that the HM/N system should be very suitable for generating spin currents.

III. RESULTS AND DISCUSSION

A. Nonlocal spin injection and detection

LSMO epitaxial thin films with a thickness of 10 nm were grown on $(LaAlO_3)_{0.3}(Sr_2TaAlO_6)_{0.7}$ (LSAT) crystal substrates in an off-axis sputtering system, and their properties were analyzed comprehensively (see device fabrication procedure and Fig. S2 within the SM [32] for more details; also Refs [35,36]). The small thickness proved essential to have electrodes with good magnetization switching characteristics. Device structures were made using electron beam lithography together with ion beam etching (see SM [32]), and bridged by a Ag nanowire, forming a lateral nonlocal configuration, as shown in Fig. 1(d). The bottom LSMO wire has two pads at the end, and is wider than the top LSMO nanowire, in order to create distinguishing coercive fields and thus set up well-defined parallel or antiparallel configurations. A 100-μA DC current was applied on the bottom wire (the spin injector) to generate spin accumulation, and the nonlocal signal was probed by the top wire (spin detector) using a voltmeter.

Prior to acquiring ΔR, the parallel state was prepared by saturating the magnetization of the nanostructures with an IP magnetic field of 1 T parallel to the wire axis, called the x axis in Fig. 1(a). The long axis of the Ag nanowire connecting the LSMO wires corresponds to the y axis. Next, ΔR was measured by sweeping the field from a positive to a negative value, and vice versa after –1 T reinitialization. Figure 1(e) shows that nonlocal spin signals were detected unambiguously from 10 K up to 200 K. At 10 K, the sharp switching of the nonlocal voltage occurred symmetrically with respect to the zero field around ±7.5 mT and returned to the initial level around ±12 mT. ΔR was calculated to be 5 mΩ at 10 K and decreased monotonically with increasing temperature. No other switching was detected in magnetic fields up to 100 mT (Fig. S3a within the SM [32]; see also Refs. [37–39]).

Interestingly, when the field direction was set in-plane and perpendicular to the long axis of both injector and detector, ΔR showed two switches (Fig. S3b within the SM [32]), although with smaller values. This can be explained by the sequential magnetization switching of pad and nanowires as explained in the SM. Moreover, the temperature dependence of MR curves of the detector (Fig. S5 within the SM [32]; see also Ref. [40]) and injector (Fig. S6 within the SM [32]) demonstrate that the coercive field difference persists up to 300 K, although the coercive fields become smaller with increasing temperature. This is summarized in Fig. S7 within the SM [32] and accounts for the trend of the diminishing ΔR in Fig. 1(e). Consequently, we ascribe the absence of a visible room-temperature (RT) ΔR to the degradation of the magnetization of the LSMO nanostructures, plus possibly strong electron-phonon scattering in the Ag nanowire near RT [31,33].

B. Hanle precession analyses

The spins flowing in the bridging Ag nanowire can precess about the axis of an applied OP field $B_\perp$, the so-called Hanle precession. The spin detector probes the spin projection on its own magnetization direction, leading to a modulation of $V(B_\perp)$ that contains information on the spin diffusion length and the spin polarization [7,19]. Figure 2(a) shows typical Hanle precession curves for a device of 377-nm length in the P (blue curve) and AP (orange curve) configurations, and also the polynomial background signal. Prior to applying the OP field, either a 1-T IP field or –1-T IP field was applied to achieve the P, AP states. Subsequently, the voltage was measured by varying the OP field. Starting from a P configuration, the signal decreases when sweeping $B_\perp$ up or down, and reaches a minimum of around ±300 mT. The maximum can be recovered at a saturating OP field of –1 T, as shown in Fig. S8 within the SM [32] (see also Refs. [18,20,24,41]). In this case, all spins are aligned, in agreement with previous observations [7,42]. We analyze the Hanle precession data

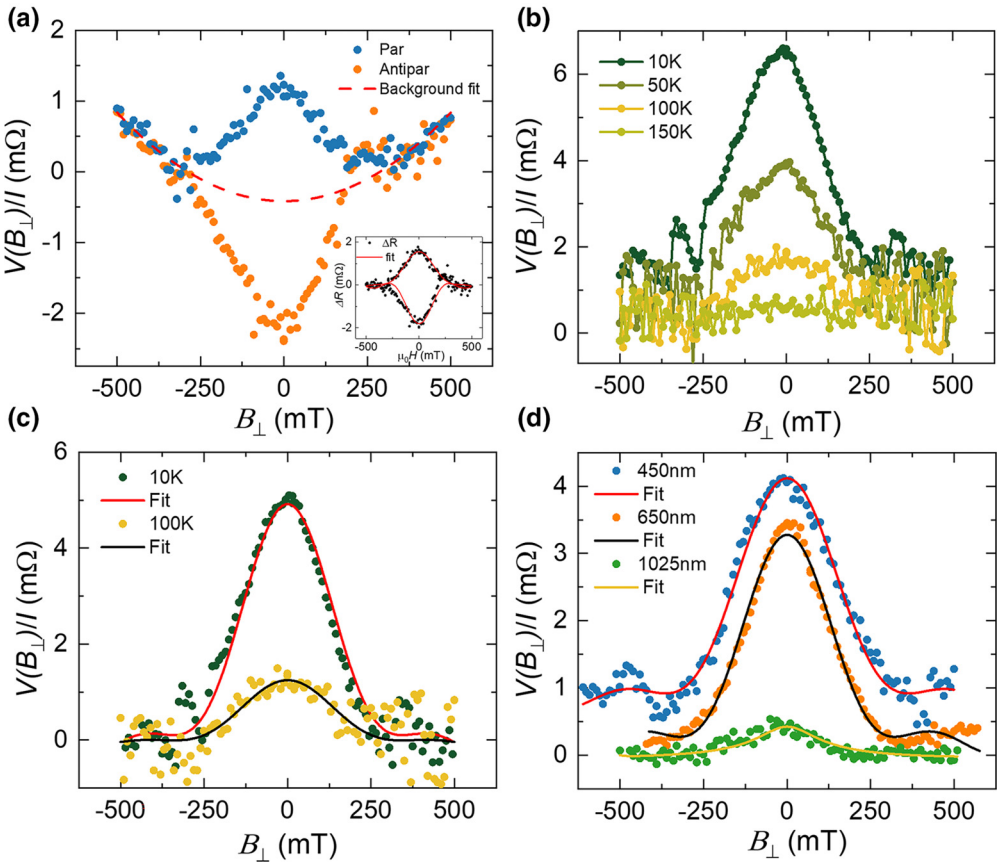

FIG. 2. Hanle precession analyses. (a) Hanle precession signals measured in parallel (olive circles) and antiparallel (orange circles) configurations in a device with 377 nm spacing. The red dashed line is the polynomial background fit. The inset shows the Hanle curves after background subtraction (black circles) and relevant fit (red curve) using Eq. (3). Temperature-dependent Hanle precession measurements in a device with 260-nm spacing (b) are fitted at 10 K (red curve) and 100 K (black curve) and plotted in (c), respectively. (d) Hanle precession measurements in devices with 450 nm (olive circles), 650 nm (orange circles), and 1025 nm (blue circles) spacing at 10 K, and corresponding fits. (b) and (d) are plotted with offsets for clarity.

numerically with the 1D diffusion model and the formula [7]

$$\frac{V(B_\perp)}{I} = \frac{P^2}{e^2 NA}\int_0^\infty \left[\frac{1}{\sqrt{4\pi Dt}}\right]\exp\left[\frac{-L^2}{4Dt}\right] \times \cos(\omega_L t)\exp\left[\frac{-t}{\tau_N}\right]dt, \quad (3)$$

where $\omega_L = g\mu_B B/\hbar$, $D = \sigma/e^2 N$, $\tau_N = \lambda_N^2 D$, P is the induced spin polarization, e is the elementary charge, N is the density of states at the Fermi energy, A is the cross-sectional area, L is the distance between the electrodes, D is the electron diffusion constant and τ_N represents the spin lifetime in the normal metal [7,8,16]. The term $P^2/e^2 NA$ describes the spin injection rate, $P(t) = [1/\sqrt{4\pi Dt}]\exp[-L^2/4Dt]$ is a spin diffusion function defining the diffusion of injected spins over time t. The precession is captured by $\cos\omega_L t$, and the exponential factor $\exp[-t/\tau_N]$ takes account of the effect of spin flipping.

The fit for the 377-nm device is shown in the inset of Fig. 2(a) after polynomial background subtraction [43]. The extracted spin lifetime τ_N is about 50 ps, and P is about 9.4%. The obtained P is much smaller than the values suggested by the calculations for the HM/N case [Fig. 1(b)]. Here we note that a low contact resistance (as opposed to the resistance of a tunnel junction) may lead to contact-induced spin relaxation and influence the nonlocal signal [18]. We will return to this issue below. We also fitted the Hanle precession data to a Lorentzian model, which is given by $\Delta\mu(B) = \Delta\mu(0)/(1 + (\omega_L\tau)^2)$ [41], describing the precessional dephasing of the spin accumulation $\Delta\mu$. Here, $\Delta\mu(0)$ is the maximum at zero field, ω_L is the Larmor frequency, and τ_N is the spin lifetime. The Lorentzian fit gives a spin lifetime $\tau_N \approx 49$ ps (Fig. S9 within the SM [32]), which is consistent with the result of the 1D diffusion model.

To gain further insight into the spin injection process, we measured the Hanle precession for a series of temperatures up to 200 K [Fig. 2(b)] and with various device lengths [Fig. 2(d)]. The amplitude of the signal decreases with temperature as already seen in Fig. 1(e), due to the weakening magnetization of LSMO nanostructures. Fits using Eq. (3), on a device with a length of 260 nm, are given in Fig. 2(c). At 10 K, there is a small deviation between the experimental data and the theoretical fit, which is probably due to the magnetization misalignment between the injector and detector, or to a small IP component of the applied OP field. Since the LSMO pad has a relatively small coercive field of 5 mT, such an IP component may induce a canted magnetization, leading to the well-known oblique Hanle precession [16,41,44,45].

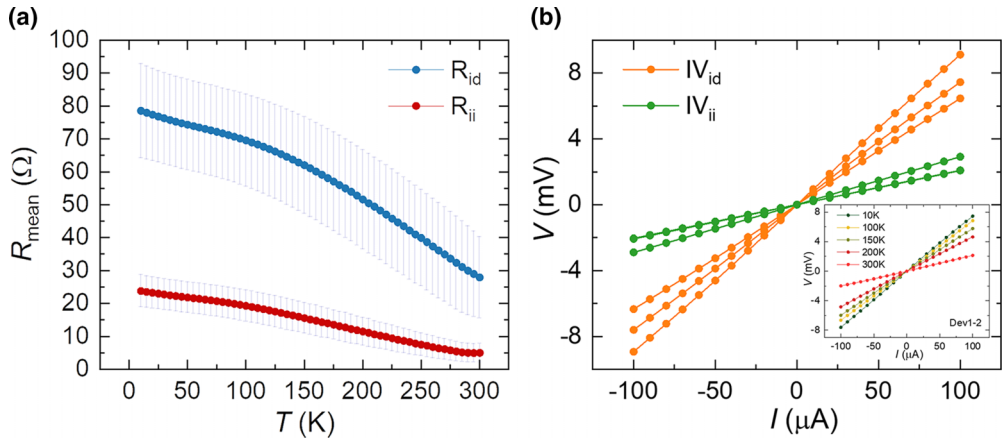

FIG. 3. Overview of interface property. The interface resistances between the detector (R_{id}) or injector (R_{ii} and the Ag nanowire of the three devices are measured as function of temperature. In (a) are plotted the averaged resistances R_{mean} for both interfaces. The error bars represent the data variations. (b) IV curves of the interfaces collected at 10 K, both for the detector (IV_{id}) and the injector (IV_{ii}). The inset in (b) shows the temperature variation of the IV characteristics for the detector interface of one selected device (Dev1-2).

After shifting the maximum of the Hanle precession curves to the point of zero field, the spin polarization is found to be 11.6% at 10 K and decreases to 5.8% at 100 K. The spin lifetime is about 65 ps at 10 K. The fitted D is 0.0025 m^2/s. According to $\lambda_N = \sqrt{D\tau_N}$, λ_N is calculated to be 405 nm at 10 K, and 360 nm at 100 K, respectively. We then examined other devices with different spacings at 10 K. As shown in Fig. 2(d), Hanle precession signals decay as spacings become larger. For lengths of 450 nm, 650 nm, and 1025 nm, the fits give 10%, 9.6%, and 7.5% spin polarization and 61 ps, 76 ps, and 62 ps spin lifetime, respectively. Using the Einstein relation $\sigma_N = e^2ND$, and the fitted value for $D \approx 0.0025\ m^2/s$ the resistivity of the Ag nanowire at 10 K is calculated to be 16 μΩ cm. For Ag, a value of around 2 μ Ωcm is expected [19], and therefore we employed a crossbar method and four-probe scheme to determine the resistivities of the LSMO and the Ag nanowires (Fig. S10 within the SM [32]). The measured ρ_{LSMO} is 232 μΩ cm, and $\rho_{Ag} \approx 18\ \mu\Omega$ cm at 10 K. Moreover, we find that for a pure Ag nanostructure grown on an LSAT substrate, ρ_{Ag} is nearly 30 μΩ cm at 10 K. This suggests that the growth on LSAT leads to a rather grainy nanowire.

C. Effects of the interface resistance R_{int}

In the introduction, we argued that, for our LSMO/Ag system, conductivity mismatch is not an issue, and that insertion of a high interface resistance in order to improve the spin injection efficiency is not required. However, the value we obtain for P from the Hanle precession analysis is quite low. Moreover, also the Hanle precession, meaning the field dependence of the nonlocal resistance, depends on the contact resistance [18]. Therefore, we measured the interface resistance of a number of our devices, by using one arm of the Ag and LSMO as current lead, and the other of each as voltage contact. The results are shown in Fig. 3. The interface resistance between the detector and the Ag nanowire (R_{id}) at 10 K is about 80 Ω on average and gradually decreases with increasing temperature [see Fig. 3(a)]. This behavior is generally regarded as the property of a nonmetallic interface. Similar behavior is observed at the interface between the injector and the Ag nanowire (R_{ii}). The interface resistance between the injector and nanowire R_{ii} is around 25 Ω at 10 K, which is reasonable because the contact area on the injector side is larger than that on the detector side. We also examined the I-V characteristics of the interfaces of three devices. All I-V's show linear behavior at 10 K [Fig. 3(b)]. Also at higher temperatures, the dependence is linear dependence [inset in Fig. 3(b)].

From these data we conclude that a resistive barrier layer is present at the interface, presumably due to the intrinsic imperfect contact or *ex situ* fabrication procedure [46]. This may also be the origin of the high resistivity of the Ag nanowire, i.e., the Ag nanowire contacting LSMO nanostructure oxidizes due to oxygen diffusion or degrades upon exposure to air, as well as nonpreferential growth on LSAT substrate.

In order to gauge the effect of the interface resistance on the behavior of the device, the values have to be compared to those of the spin resistances $R_N = \rho_N\lambda_N/A_N$ and $R_F = \rho_F\lambda_F/A_F$ of the Ag and the LSMO, respectively. Here, $\lambda_{N(F)}$ are the spin diffusion lengths in the normal metal (ferromagnet) and $A_{N(F)}$ the cross section of the normal metal (ferromagnet). We use $\rho_{Ag} \approx 20\ \mu\Omega$ cm, $\rho_{\text{LSMO}} \approx 232\ \mu\Omega$ cm, λ_N is 405 nm, λ_F is 2.6 nm [30,47], A_N is 0.05*0.8 μm^2, A_F is 0.01*1.5 μm^2, and calculate the corresponding R_N and R_F to be 2 Ω and 0.4 Ω at 10 K approximately. Clearly, the contact resistance is significantly larger than the spin resistance. As one important consequence, this validates using the standard Hanle formula without taking contact-induced effects into account [18]. In order to quantify contact effects, Ref. [18] introduced an R parameter, defined as $(R = (R_{\text{int}}/\rho_{Ag})A)$, with A the cross section of the Ag nanowire. Contact effects become important when $R/\lambda_N \ll 1$ and $L/\lambda_N \ll 1$. With our experimental values, we obtain $R/\lambda_N \approx 14$, and $L/\lambda_N \leqslant 1$, ensuring reliable Hanle precession results (see SM [32] for more details).

Another consequence is that the assumption of a transparent interface is not correct (see SM [32] for more details). Instead, we should analyze the dependence of ΔR on the length between the contacts L by the formula [7,23]

$$R_S = \Delta R = P^2 R_N \exp[-L/\lambda_N] \quad (4)$$

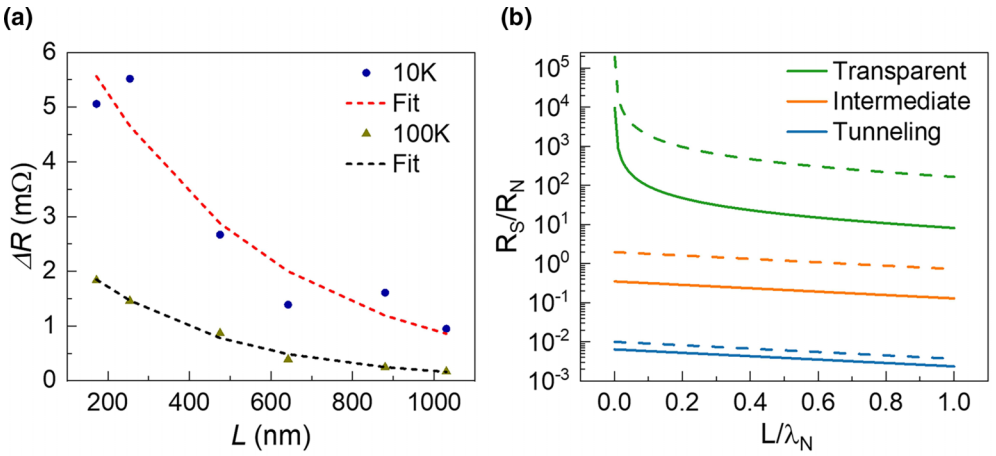

FIG. 4. Spin transport as a function of the spacing between contacts L. (a) Experimental spacing-dependent nonlocal signals at 10 K (blue circles) and 100 K (yellow triangles). The red-dashed and black-dashed lines are fits appropriate for the tunnel regime using Eq. (4). (b) Calculations of the spin resistance R_S normalized by the resistance of the normal metal R_N as function of L, normalized by the spin diffusion length λ_N, for the tunneling, intermediate and transparent regimes. Solid lines are calculations of R_S based on the experimental and fitted parameters, dashed lines represent calculations using ideal parameters for the Ag bridge.

where P is the induced spin polarization, and R_N is computed from the values for A_N and ρ_N given above. Values for $\Delta R(L)$ at 10 K and 100 K are plotted in Fig. 4(a), together with the fit to Eq. (4). We find $P \approx 8\%$, $\lambda_N \approx 460$ nm at 10 K, and $P \approx 5.4\%$, $\lambda_N \approx 350$ nm at 100 K, respectively. Moreover, the spin lifetime can be computed with $\sigma_N = e^2 N D$ and $\lambda_N = \sqrt{D\tau_N}$, yielding 70 ps and 46 ps at 10 K and 100 K. All values are in good agreement with the values extracted from the Hanle precession analyses.

D. Discussion of the transport data

According to the model calculations we presented in the Introduction, injecting spin-polarized electrons from LSMO into a normal metal channel could yield a large nonlocal spin signal and a high-induced spin polarization. The experiments, however, although producing clear nonlocal signals, show quite low values. In particular, the extracted spin polarization P from the Hanle precession model is lower than the theoretical calculations indicate. By examining the interface resistivity, we find the presence of an interfacial barrier layer. This is quite common. For LSMO/Pt contacts, values of $5 \times 10^{-9}\,\Omega\mathrm{m}^2$ were reported [46], substantially higher still than what we find, of order $2.5 \times 10^{-11}\,\Omega\mathrm{m}^2$. Being in the tunneling regime, however, is in itself not an explanation for the loss of spin polarization. We have to conclude that the interface is not only a resistive barrier, but also a spin scatterer [23,48]. This led us to an investigation of the interface with scanning transmission electron microscopy (STEM). The STEM data, shown below, corroborate the conclusions from the transport data. Before going there, we finish the discussion on the transport data by elaborating on the effects that an improved interface would have, by considering what could be expected in the intermediate and transparent regimes.

In the intermediate regime, when either R_{ii} or R_{id} is larger than (R_F) and (R_N), i.e., $(R_{ii} \ll R_F,\ R_N \ll R_{id})$ or $(R_{id} \ll R_F, R_N \ll R_{ii})$, the expression for the spin resistance R_S is given by [23]

$$R_S = \frac{2P_F P}{1 - P_F^2} R_N \frac{R_F}{R_N} \exp[-L/\lambda_N]. \tag{5}$$

In the transparent regime, when $R_{\mathrm{int}} \ll (R_F, R_N)$, R_S is given by

$$R_S = \frac{4P_F^2}{\left(1 - P_F^2\right)^2} R_N \left(\frac{R_F}{R_N}\right)^2 \frac{\exp[-L/\lambda_N]}{1 - \exp[-2L/\lambda_N]}. \tag{6}$$

Using the experimental and fitted values, i.e., $P \approx 8\%$, $R_N \approx 2\ \Omega$, $R_F \approx 0.4\ \Omega$, $\lambda_N \approx 460$ nm, and taking $P_F = 0.96$, we can calculate the ratio R_S/R_N as function of the length between the contact L in all three regimes. As shown in Fig. 4(b) (solid lines), the ratio of R_S/R_N drops by roughly 10^6 when going from the transparent regime to the tunneling regime. Note the interfacial spin scattering is not considered here. We also computed the spin transport in the LSMO/Ag system using optimal values for the properties of Ag, a resistivity of $\sim 2\ \mu\Omega\,\mathrm{cm}$, and a spin diffusion length $\lambda_N \approx 1\,\mu\mathrm{m}$ [19], together with $P = 0.1$ for simplicity. Those results are plotted by the dashed lines in Fig. 4(b). Two points can be made from the calculation. One is that a higher quality of the Ag would affect the size of the nonlocal signal, but would not affect the outcome in a qualitative way. The other is that, in contrast to the all-metals case, inserting a tunnel barrier would not improve the results, which is a direct consequence of the fact that conductivity mismatch does not play a role in the LSMO/Ag system. Clearly, once again, the key to improving the spin injection efficiency when using LSMO lies in a better control over both the conductance and the spin activity of the interface.

Finally, we mention a control experiment performed by replacing Ag with Pt. Pt has a very strong spin-orbit interaction due to its large atomic number and is often used as a spin absorber [3,49,50]. We find that no nonlocal signal is detectable in devices with a spacing of 200 nm, 250 nm, or 625 nm. Since the spin diffusion length of Pt is just 10 nm [50], it makes sense that no spin current is detected. It reinforces

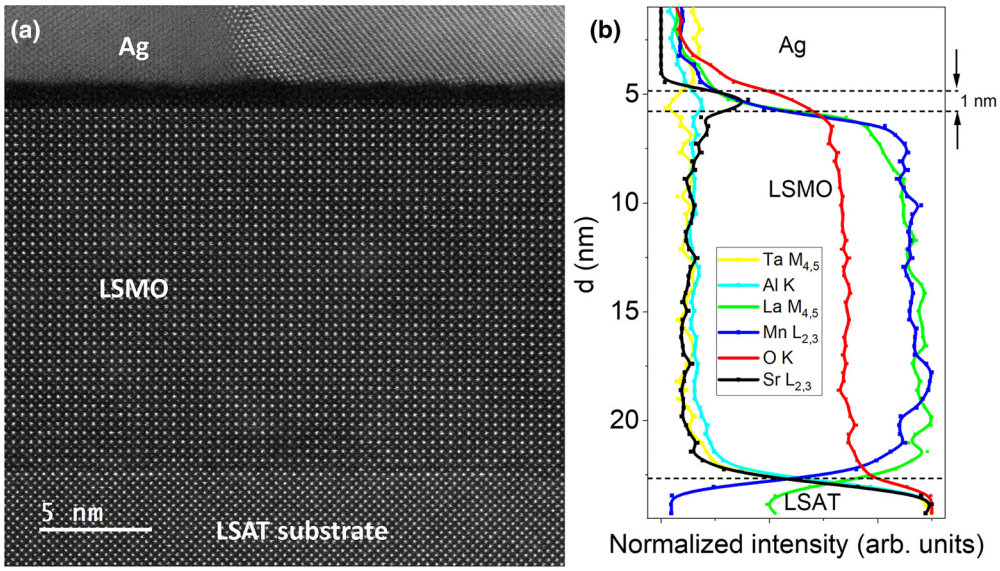

FIG. 5. (a) High-angle annular dark field image, made by scanning transmission electron microscopy, of an LSAT/LSMO/Ag sample. It shows the epitaxial LSAT/LSMO interface and the disordered LSMO/Ag interface. Two different grains are visible in the Ag layer. (b) Averaged electron energy loss chemical map showing the Ta $M_{4,5}$, Al K, La $M_{4,5}$, Mn $L_{2,3}$, O K, and Sr $L_{2,3}$ intensity profiles of the layers. Dashed lines indicate the LSAT/LSMO and LSMO/Ag interfaces.

the assertion that there are no spurious magnetoresistance contributions to our measured nonlocal spin signal (see also Fig. S11 within the SM [32]).

E. STEM inspection of the interface

Aberration corrected scanning transmission electron microscopy (STEM) combined with electron energy loss spectroscopy (EELS) has been performed to study the structural and chemical properties of the sample. The STEM-EELS data were acquired at 200 kV in a JEOL ARM200cF microscope equipped with a spherical aberration corrector and a Gatan Quantum Dual-EELS spectrometer. Figure 5(a) displays a high angle annular dark field image showing the high quality of the different layers. The 15-nm LSMO layer is epitaxial, atomically smooth and free of disorder over the entire thickness. The Ag layer contains grains, as can also seen in Fig. S12a within the SM [32]. The LSMO/Ag boundary shows a dark contrast typical of an incoherent interface or due the presence of a thin layer with lower atomic weight [51]. The termination of both LSAT/LSMO and LSMO/Ag interfaces were analyzed using electron energy loss spectroscopy. Figure 5(b) shows a chemical profile of the layers from an averaged electron energy loss spectrum image, measured by the normalized intensities at the ionization edges of Ta $M_{4,5}$, Al K, La $M_{4,5}$, Mn $L_{2,3}$, O K, and Sr $L_{2,3}$. From the profiles, the interfaces are observed to be chemically sharp with LaO/MnO2 as expected. On the other side, the LSMO/Ag interface shows that the Mn $L_{2,3}$ and La $M_{4,5}$ edge signals vanish 1 nm before the O K edge signal. At the same time, a small and not negligible Sr signal rises at the interface, suggesting that extra SrO planes may be present between the LSMO layer and the Ag capping. No significant decrease of the Mn valency is observed up to the onset of the disordered layer (Fig. S12b within the SM [32]) but the presence of Mn in thin layer cannot be ruled out, and finding spin scattering in this disordered interface seems quite plausible.

IV. CONCLUSIONS

In summary, we have presented experiments on the electrical injection and detection of a pure spin current in lateral LSMO/Ag spin valves. We show that the high spin polarization combined with the high resistivity of the LSMO could make the spin injection very efficient. However, from analyzing Hanle precession data and the spatial decay of the signal, both at 10 K, we find values for the spin polarization P in the Ag of the order of 10%, which is quite low. Signals can be obtained up to 200 K. At higher temperatures, the degrading magnetization, changes in the anisotropy as well as the strong electron-phonon scattering in the Ag channel make the detection difficult. With respect to the low P, We argue that an interfacial spin-active layer hinders effective injection, and TEM data support that conclusion. Since the interfaces of oxides are notoriously difficult to control, this is a significant hindrance in using the otherwise promising properties of the LSMO. Still, there may be instances where the availability of a simple injection system is an asset.

ACKNOWLEDGMENTS

The authors thank Kaveh Lahabi for discussions, and Prateek Kumar, Marcel Hesselberth and Douwe Scholma for support in device preparation and measurements. Y.J. is funded by China Scholarship Council (Grant No. 201808440424). The research is financially supported by the Dutch Research Council (NWO) through Projectruimte Grant No. 680.91.128. We also thank the ICTS-Centro Nacional de Microscopía for the use of its facilities.

[1] I. Žutić, J. Fabian, and S. Das Sarma, Rev. Mod. Phys. **76**, 323 (2004).

[2] A. Hirohata, K. Yamada, Y. Nakatani, I.-L. Prejbeanu, B. Diény, P. Pirro, and B. Hillebrands, J. Magn. Magn. Mater. **509**, 166711 (2020).

[3] S. O. Valenzuela and M. Tinkham, Nature (London) **442**, 176 (2006).

[4] G. E. W. Bauer, E. Saitoh, and B. J. van Wees, Nat. Mater. **11**, 391 (2012).

[5] D. H. Hernando, Y. V. Nazarov, A. Brataas, and G. E. W. Bauer, Phys. Rev. B **62**, 5700 (2000).

[6] F. J. Jedema, A. T. Filip, and B. J. van Wees, Nature (London) **410**, 345 (2001).

[7] F. J. Jedema, H. B. Heersche, A. T. Filip, J. J. Baselmans, and B. J. van Wees, Nature (London) **416**, 713 (2002).

[8] F. J. Jedema, M. V. Costache, H. B. Heersche, J. J. A. Baselmans, and B. J. van Wees, Appl. Phys. Lett. **81**, 5162 (2002).

[9] M. Johnson and J. Byers, Phys. Rev. B **67**, 125112 (2003).

[10] H. Idzuchi, Y. Fukuma, and Y. Otani, Physica E **68**, 239 (2015).

[11] S. M. Watts, J. Grollier, C. H. van der Wal, and B. J. van Wees, Phys. Rev. Lett. **96**, 077201 (2006).

[12] Y. Tserkovnyak, A. Brataas, and G. E. W. Bauer, Phys. Rev. B **66**, 224403 (2002).

[13] S. M. Watts, J. Grollier, C. H. van der Wal, and B. J. van Wees, Phys. Rev. B **59**, 11465 (1999).

[14] M. V. Costache, M. Sladkov, S. M. Watts, C. H. van der Wal, and B. J. van Wees, Phys. Rev. Lett. **97**, 216603 (2006).

[15] T. Kimura and Y. Otani, Phys. Rev. Lett. **99**, 196604 (2007).

[16] F. Rortais, C. Vergnaud, A. Marty, L. Vila, J. P. Attané, J. Widiez, C. Zucchetti, F. Bottegoni, H. Jaffrès, J. M. George, and M. Jamet, Appl. Phys. Lett. **111**, 182401 (2017).

[17] T. Kimura, J. Hamrle, and Y. Otani, Phys. Rev. B **72**, 014461 (2005).

[18] T. Maassen, I. J. Vera-Marun, M. H. D. Guimarães, and B. J. van Wees, Phys. Rev. B **86**, 235408 (2012).

[19] Y. Fukuma, L. Wang, H. Idzuchi, S. Takahashi, S. Maekawa, and Y. Otani, Nat. Mater. **10**, 527 (2011).

[20] O. M. van 't Erve, A. L. Friedman, C. H. Li, J. T. Robinson, J. Connell, L. J. Lauhon, and B. T. Jonker, Nat. Commun. **6**, 7541 (2015).

[21] G. Schmidt, D. Ferrand, L. W. Molenkamp, A. T. Filip, and B. J. van Wees, Phys. Rev. B **62**, R4790 (2000).

[22] E. I. Rashba, Phys. Rev. B **62**, R16267 (2000).

[23] S. Takahashi and S. Maekawa, Phys. Rev. B **67**, 052409 (2003).

[24] F. J. Jedema, M. S. Nijboer, A. T. Filip, and B. J. van Wees, Phys. Rev. B **67**, 085319 (2003).

[25] R. Godfrey and M. Johnson, Phys. Rev. Lett. **96**, 136601 (2006).

[26] Y. Lu, X. W. Li, G. Q. Gong, G. Xiao, A. Gupta, P. Lecoeur, J. Z. Sun, Y. Y. Wang, and V. P. Dravid, Phys. Rev. B **54**, R8357 (1996).

[27] V. Garcia, M. Bibes, A. Barthélémy, M. Bowen, E. Jacquet, J.-P. Contour, and A. Fert, Phys. Rev. B **69**, 052403 (2004).

[28] G. Y. Luo, C. R. Chang, and J. G. Lin, J. Appl. Phys. **115**, 17C508 (2014).

[29] G. Y. Luo, J. G. Lin, W.-C. Chiang, and C.-R. Chang, Sci. Rep. **7**, 6612 (2017).

[30] W. Yan, L. C. Phillips, M. Barbone, S. J. Hamalainen, A. Lombardo, M. Ghidini, X. Moya, F. Maccherozzi, S. van Dijken, S. S. Dhesi, A. C. Ferrari, and N. D. Mathur, Phys. Rev. Lett. **117**, 147201 (2016).

[31] G. Mihajlovic, J. E. Pearson, S. D. Bader, and A. Hoffmann, Phys. Rev. Lett. **104**, 237202 (2010).

[32] See Supplemental Material at http://link.aps.org/supplemental/10.1103/PhysRevMaterials.7.104408 for additional details as indicated in the main text.

[33] H. Idzuchi, Y. Fukuma, L. Wang, and Y. Otani, Appl. Phys. Lett. **101**, 022415 (2012).

[34] Y. Cai, C. Qin, F. Kandaz, X. Shen, C. Zhou, M. Jia, Y. Luo, Y. Wu, and Y. Ji, Phys. Rev. B **100**, 144419 (2019).

[35] N. Mottaghi, M. S. Seehra, R. Trappen, S. Kumari, C.-Y. Huang, S. Yousefi, G. B. Cabrera, A. H. Romero, and M. B. Holcomb, AIP Adv. **8**, 056319 (2018).

[36] H. Boschker, M. Huijben, A. Vailionis, J. Verbeeck, S. van Aert, M. Luysberg, S. Bals, G. van Tendeloo, E. P. Houwman, G. Koster *et al.*, J. Phys. D: Appl. Phys. **44**, 205001 (2011).

[37] X. Zou and G. Xiao, Phys. Rev. B **77**, 054417 (2008).

[38] M. S. Anwar and J. Aarts, Phys. Rev. B **88**, 085123 (2013).

[39] D. Fadil, S. Wu, P. Perna, B. Renault, M. Saïb, S. Lebargy, J. Gasnier, B. Guillet, J.-M. Routoure, S. Flament *et al.*, J. Appl. Phys. **112**, 013906 (2012).

[40] I. A. Malik, H. Huang, Y. Wang, X. Wang, C. Xiao, Y. Sun, R. Ullah, Y. Zhang, J. Wang, M. A. Malik *et al.*, Sci. Bull. **65**, 201 (2020).

[41] S. P. Dash, S. Sharma, R. S. Patel, M. P. de Jong, and R. Jansen, Nature (London) **462**, 491 (2009).

[42] M. Popinciuc, C. Józsa, P. J. Zomer, N. Tombros, A. Veligura, H. T. Jonkman, and B. J. van Wees, Phys. Rev. B **80**, 214427 (2009).

[43] X. Lou, C. Adelmann, S. A. Crooker, E. S. Garlid, J. Zhang, K. S. M. Reddy, S. D. Flexner, C. J. Palmstrøm, and P. A. Crowell, Nat. Phys. **3**, 197 (2007).

[44] C. Awo-Affouda, O. M. J. van 't Erve, G. Kioseoglou, A. T. Hanbicki, M. Holub, C. H. Li, and B. T. Jonker, Appl. Phys. Lett. **94**, 102511 (2009).

[45] K.-R. Jeon, B.-C. Min, Y.-H. Park, S.-Y. Park, and S.-C. Shin, Phys. Rev. B **87**, 195311 (2013).

[46] M. Abuwasib, H. Lee, A. Gruverman, C.-B. Eom, and U. Singisetti, Appl. Phys. Lett. **107**, 242905 (2015).

[47] The spin diffusion length (or spin-flip time) is that of the out-of-equilibrium spin, and therefore very short in a half-metal where the empty spin band is much higher in energy.

[48] J. Bass and W. P. Pratt, J. Phys.: Condens. Matter **19**, 183201 (2007).

[49] T. Kimura, Y. Otani, T. Sato, S. Takahashi, and S. Maekawa, Phys. Rev. Lett. **98**, 156601 (2007).

[50] D. A. Abanin, A. V. Shytov, L. S. Levitov, and B. I. Halperin, Phys. Rev. B **79**, 035304 (2009).

[51] S. J. Pennycook and L. A. Boatner, Nature (London) **336**, 565 (1988).